MADRID
inter.noise 2019
June 16 - 19
NOISE CONTROL FOR A BETTER ENVIRONMENT

Validation of a model for acoustic absorption in porous media

Satcunanathan, Sutharsan[1]; Zamponi, Riccardo[2]; Meinke Matthias[3]; Van de Wyer, Nicolas[4]; Schram, Christophe[5]; Schröder, Wolfgang[6]

[1,3,6]Chair of Fluid Mechanics and Institute of Aerodynamics
Wüllnerstr. 5a, 52062 Aachen, Germany

[2,4,5]von Karman Institute for Fluid Dynamics
Waterloosesteenweg 72, 1640 Sint-Genesius-Rode, Belgium

ABSTRACT

The analysis of porous materials for aeroacoustic noise mitigation requires high-fidelity numerical tools to simulate the sound propagation and interaction in porous media. The manuscript presents the calibration and validation of a direct-hybrid LES/CAA method used to model the aerodynamically generated sound. The porous micro-structures are modeled with a volume-averaging approach. Additional terms, emerging in the governing equations, owing to the force exerted by the porous matrix on the fluid, are closed by means of Darcy's law and the quadratic Forchheimer term. The sound generation and propagation is predicted by a solution of the acoustic perturbation equations via a discontinuous Galerkin method. The model for the porous material is separately calibrated for the CFD and CAA with the parameters retrieved by the characterization of a melamine foam in experimental tests. The sound predicted by an absorbing layer of the material is compared with measurements performed in an impedance tube. Secondly, the transmission coefficient of the melamine foam placed in an acoustic liner configuration inside a duct is studied numerically. The results are then compared with experiments conducted in absence of a flow and also with a flow velocity of 30 **m/s in order to assess the accuracy of the model calibration.**

Keywords: Modelling, Porous materials, Acoustic absorption
I-INCE Classification of Subject Number: 76
(see http://i-ince.org/files/data/classification.pdf)

[1]s.satcunanathan@aia.rwth-aachen.de
[2]riccardo.zamponi@vki.ac.be

1. INTRODUCTION

In the current work, sets of equations to be used in flow and acoustic simulations of porous media are presented in the compressible framework. This involves the Darcy-Forchheimer model, which has been extensively used for incompressible flow simulations [1], but only recently applied for acoustic predictions [2–4]. The model assumes a rigid porous frame, i.e. no elastic coupling effects are taken into account. For simple homogeneous porous materials with porosity and tortuosity close to one, as considered here, it is assumed that the parameter that mostly influences the acoustic behavior of the material is the flow resistivity [5].

For its validation, the model has been firstly calibrated considering a sample of melamine foam and then applied to different configurations for analyzing the sound absorbing behavior of the material and for studying the transmission and the reflection coefficients in a liner configuration. The calibration procedure requires the knowledge of the parameters of the porous medium, that can be retrieved through the experimental characterization of the sample based on impedance tube measurements. According to the semi-phenomenological model of Johnson-Champoux-Allard-Lafarge (JCAL) [6], the six parameters considered necessary to fully characterize the material are the static air flow resistivity, σ, the porosity, ϵ, the tortuosity, α_∞, the viscous characteristic length, Λ, the thermal characteristic length, Λ' and the thermal permeability, κ_0'. Beside these, another parameter that is used to define a porous medium is the viscous permeability, κ_0, which is directly linked to σ.

In Chapter 2 the model equations for porous media for the flow and acoustic fields are presented and analyzed for the case of plane waves. Chapter 3 introduces the experimental setups, which are considered in Chapter 4 to evaluate the model.

2. MODELING OF THE POROUS MEDIA

The numerical part of the present work relies on a hybrid two-step CFD/CAA approach for the prediction of aerodynamically generated noise, where the former provides the mean flow field and acoustic sources for the subsequent CAA simulation, which accounts for effects, like convection, refraction, diffraction and scattering of acoustic waves. This enables for both an optimal choice of the respective numerical solvers, preferably a high order scheme for the CAA, and differing mesh resolutions to cope with the large disparity in the turbulent and acoustic scales.

In the remainder of this chapter, the model equations for the porous media are derived for the flow and acoustic part. Finally, the model is theoretically analyzed for the simple case of a plane wave propagation in the limit of vanishing mean flow, in terms of the complex impedance, the complex wave number and the complex reflection coefficient at the fluid-porous interface.

2.2.1. Volume Averaged Navier Stokes Equations for the CFD

The full resolution of the porous micro-structures, e.g. in the order of $O(100\,\mu\text{m})$, for a realistic setup is beyond today's computing power. Thus, it is state-of-the-art to apply the method of volume averaging [1, 7, 8] and treat the air-saturated porous media as a homogeneous phase, to effectively account for the integral effects of the porous matrix on the possibly turbulent flow field. Considerable work has been devoted in the past to derive the equations for the incompressible flow, including special treatments for the change

in material parameters at the fluid-porous interface by e.g. either the variable porosity model [2,9] or a momentum transfer condition formulated as a jump condition across the interface as suggested in [10]. Since a careful derivation in the compressible framework is rare, it will be briefly outlined in the following:
The volume averaging operation, acting as a spatial filter, for a quantity ϕ is defined as:

$$\langle\phi\rangle^s = \frac{1}{V}\int_{V_f}\phi d\mathbf{V} = \epsilon\langle\phi\rangle \quad \text{with} \quad \langle 1\rangle^s = \epsilon, \tag{1}$$

$$\langle\phi\rangle = \frac{1}{V_f}\int_{V_f}\phi d\mathbf{V}, \tag{2}$$

where $\epsilon \in [0,1] \neq f(t)$ for a rigid porous material, $\langle\ \rangle^s$ denotes superficial average, $\langle\ \rangle$ intrinsic average and $V_f = \epsilon V$ is the volume occupied by the fluid phase. V can be conveniently considered as a filter size which scales with the characteristic length of the pores. To express the derivatives in the governing equations in terms of averaged quantities rather than averaged derivatives, the spatial averaging theorem and the commutation of the time derivative and averaging is employed [8]:

$$\langle\nabla\phi\rangle^s = \nabla\langle\phi\rangle + \frac{1}{V}\int_{A_{fs}}\mathbf{n}\phi dA, \tag{3}$$

$$\left\langle\frac{\partial}{\partial t}\right\rangle = \frac{\partial}{\partial t}\langle\ \rangle, \tag{4}$$

with A_{fs} denoting the fluid-solid interfacial area in the porous media. The Favre average of the velocity relates to the superficial and intrinsic averages as follows:

$$\langle u_i\rangle_F = \frac{\langle\rho u_i\rangle}{\langle\rho\rangle} = \frac{\langle\rho u_i\rangle^s}{\langle\rho\rangle^s} \quad \text{with} \quad u_i = \langle u_i\rangle_F + u_i^{''}. \tag{5}$$

Applying Equations 1 - 5 to the compressible Navier-Stokes equations and taking into account the no-slip condition one obtains for the mass conservation:

$$\frac{\partial\langle\rho\rangle}{\partial t} + \frac{\partial}{\partial x_j}\left(\langle\rho\rangle\langle u_j\rangle_F\right) + \langle\rho\rangle\langle u_j\rangle\frac{\partial}{\partial x_j}\ln\epsilon = 0. \tag{6}$$

The same procedure applied to the momentum equation yields in a first step:

$$\begin{aligned}\frac{\partial}{\partial t}\left(\langle\rho\rangle\langle u_i\rangle_F\right) + \frac{\partial}{\partial x_j}\left(\langle\rho\rangle\langle u_i\rangle_F\langle u_j\rangle_F\right) + \frac{\partial\langle p\rangle}{\partial x_i} - \frac{\partial\langle\tau_{ij}\rangle^s}{\partial x_j} + \langle\rho\rangle\langle u_i\rangle_F\langle u_j\rangle_F\frac{\partial}{\partial x_j}\ln\epsilon + \\ +\langle p\rangle\frac{\partial}{\partial x_i}\ln\epsilon + \frac{\partial}{\partial x_j}\left(\langle\rho u_i u_j\rangle^s - \langle\rho\rangle^s\langle u_i\rangle_F\langle u_j\rangle_F\right) + \frac{1}{V}\int_{A_{fs}} n_j(p\delta_{ij} - \tau_{ij})dA = 0,\end{aligned} \tag{7}$$

where the usual notations for the Kronecker delta δ_{ij} and the viscous stress tensor τ_{ij} have been used. Following the discussion in [11], the spatial correlations in the unresolved variations, the subgrid-scale stresses in an LES, are neglected. The surface integral accounts for the presence of the solid phase, exerting a force on the fluid. It is further assumed that the molecular transport properties vary negligibly over the averaging volume. Using Equation 1, the integral can be reformulated:

$$\frac{1}{V}\int_{A_{fs}} n_j(p\delta_{ij} - \tau_{ij})dA \approx -\langle p\rangle\frac{\partial}{\partial x_j}\ln\epsilon + \langle\tau_{ij}\rangle_F\frac{\partial}{\partial x_j}\ln\epsilon + \underbrace{\frac{1}{V}\int_{A_{fs}} n_j(p^{'}\delta_{ij} - \tau_{ij}^{''})dA}_{:=\mathcal{F}_i}. \tag{8}$$

By splitting the gradient-porosity terms of the averages from the remaining terms, the newly emerged integral in the fluctuation quantities contains only a negligible excess contribution in non-homogenous regions. The problem is closed by means of Darcy's law and the Forchheimer correction term [12, 13], which, written in a non-dimensional form for an isotropic medium, reads:

$$\hat{\mathcal{F}}_i = \underbrace{\frac{1}{Re_{d_p}\sqrt{Da}}\epsilon\hat{\mu}\hat{u}_i}_{Darcy} + \underbrace{\frac{1}{\sqrt{Da}}\epsilon^2 c_F\hat{\rho}\sqrt{\hat{u}_j\hat{u}_j}\hat{u}_i}_{Forchheimer} \quad \text{with} \quad Re_{d_p} = \frac{\rho_{ref}u_{ref}d_p}{\eta_{ref}},\ Da = \frac{\kappa}{L_{ref}^2}. \tag{9}$$

$\kappa[m^2]$ is the permeability, quantifying the flow resistivity, $\sqrt{\kappa} \sim d_p$ is a measure for the effective pore diameter, c_F is the Forchheimer coefficient and $()_{ref}$ refers to some problem specific reference quantities. In a nearly incompressible flow, conservation of mass flux requires $\mathcal{O}(\epsilon\hat{u}) \sim 1$ and $\mathcal{O}(\epsilon^2\hat{u}^2) \sim 1$, such that $\mathcal{O}(Darcy) \sim 1/\sqrt{Da}Re_{d_p}$ and $\mathcal{O}(Forch.) \sim c_F/\sqrt{Da}$. The former is related to the Stokes drag, whereas the later accounts for the inertia effects at higher permeability Reynolds numbers Re_{d_p}.

Finally, the superficial average of the viscous term in Equation 7 is reformulated for a Newtonian fluid:

$$\langle\tau_{ij}\rangle^s = \epsilon\langle\tau_{ij}\rangle_F + \underbrace{\mu\left(\langle u_i\rangle_F\frac{\partial\epsilon}{\partial x_j} + \langle u_j\rangle_F\frac{\partial\epsilon}{\partial x_i} - \frac{2}{3}\langle u_k\rangle_F\frac{\partial\epsilon}{\partial x_k}\delta_{ij}\right)}_{\mathcal{A}_{ij}}, \tag{10}$$

which completes the derivation of the averaged momentum equation:

$$\begin{aligned}\frac{\partial}{\partial t}\left(\langle\rho\rangle\langle u_i\rangle_F\right) + \frac{\partial}{\partial x_j}\left(\langle\rho\rangle\langle u_i\rangle_F\langle u_j\rangle_F\right) + \frac{\partial\langle p\rangle}{\partial x_i} - \frac{\partial\langle\tau_{ij}\rangle_F}{\partial x_j} \\ +\langle\rho\rangle\langle u_i\rangle_F\langle u_j\rangle_F\frac{\partial}{\partial x_j}\ln\epsilon + \frac{\mathcal{F}_i}{\epsilon} - \frac{1}{\epsilon}\frac{\partial\mathcal{A}_{ij}}{\partial x_j} = 0.\end{aligned} \tag{11}$$

In this work the viscous gradient-porosity terms are neglected compared to the inviscid terms. Similar considerations, where the heat flux at the fluid-solid interface is omitted, leads to the volume averaged energy equation:

$$\begin{aligned}\frac{\partial}{\partial t}\left(\langle\rho\rangle\langle E\rangle_F\right) + \frac{\partial}{\partial x_k}\left(\langle u_k\rangle_F(\langle\rho\rangle\langle E\rangle_F + \langle p\rangle)\right) - \frac{\partial}{\partial x_k}\left(\langle u_j\tau_{jk}\rangle_F\right) - \frac{\partial\langle k_{d,k}\rangle}{\partial x_k} \\ +\left(\langle u_k\rangle_F(\langle\rho\rangle\langle E\rangle_F + \langle p\rangle) - \langle u_j\rangle_F\langle\tau_{jk}\rangle_F - \langle k_{d,k}\rangle\right)\frac{\partial}{\partial x_k}\ln\epsilon - \frac{1}{\epsilon}\frac{\partial}{\partial x_k}\left(\langle u_j\rangle_F\mathcal{A}_{jk}\right) = 0,\end{aligned} \tag{12}$$

where, again, the subgrid-scale stresses have been neglected. For $\epsilon = 1$ one retains the volume averaged Navier-Stokes equations without subgrid scale stresses formally identical to the equations solved in a MILES context. The difference is the requirement with respect to the filtering width in the LES compared to the filtering in a porous medium, which is dictated by the scales of the porous micro-structures. The aforementioned equations are solved for the flow field using a finite-volume method based on an advective upstream splitting method (AUSM) in combination with the monotone upstream centered scheme for conservation laws (MUSCL) for the inviscid fluxes and a centered discretization for the viscous fluxes. Both spatial formulations are second-order accurate. A low-storage explicit 5-stage Runge-Kutta method for the time integration [14–16] also of second-order accuracy is used for the time integration. The

equations are discretized on a locally refined unstructured Cartesian mesh, where a fully conservative cut-cell approach is used for the immersed boundaries [16]. The LES is based on the MILES ansatz, in which the low dissipation of the numerical methods replaces an explicit subgrid scale model. From Equations 6, 11 and 12 it can be derived, that the inviscid gradient-porosity terms describe an isotropic flow change across the interface, as was already suggested by [17, 18] for compressible flows and naturally follows from the preceding derivation. To circumvent the numerical implementation of dirac-shaped source terms and a smearing of the interface, a numerical implementation, in which the jump is directly incorporated into the flux discretization of the finite-volume method has been devised to sharply resolve the fluid-porous immersed interface on a non-interface fitted Cartesian mesh [19].

2.2.2. Volume Averaged Perturbation Equations for the CAA

The derivation of acoustic perturbation equations starts by reformulating Equations 6, 11 and 12 into equations for the intrinsic pressure $\langle p \rangle$ and the Favre-averaged velocity $\langle u_i \rangle_F$:

$$\frac{\partial \langle u_i \rangle_F}{\partial t} + \langle u_k \rangle_F \frac{\partial \langle u_i \rangle_F}{\partial x_k} + \frac{1}{\langle \rho \rangle} \frac{\partial \langle p \rangle}{\partial x_i} - \frac{1}{\langle \rho \rangle} \frac{\partial \langle \tau_{ki} \rangle_F}{\partial x_k} + \frac{1}{\langle \rho \rangle} \frac{\mathcal{F}_i}{\epsilon} = 0, \tag{13}$$

$$\begin{aligned} &\frac{\partial \langle p \rangle}{\partial t} + \langle u_k \rangle_F \frac{\partial \langle p \rangle}{\partial x_k} + \gamma \langle p \rangle \frac{\partial \langle u_k \rangle_F}{\partial x_k} - (\gamma - 1) \langle \tau_{jk} \rangle_F \frac{\partial \langle u_j \rangle_F}{\partial x_k} - (\gamma - 1) \frac{\partial \langle k_{d,k} \rangle}{\partial x_k} \\ &+ \left(\gamma \langle p \rangle \langle u_k \rangle_F - (\gamma - 1) \langle u_j \rangle_F \langle \tau_{jk} \rangle_F - (\gamma - 1) \langle k_{d,k} \rangle \right) \frac{\partial}{\partial x_k} \ln \epsilon - (\gamma - 1) \langle u_i \rangle_F \frac{\mathcal{F}_i}{\epsilon} = 0. \end{aligned} \tag{14}$$

Alternatively, spatial averaging can be applied to the p and u_i equations, but the neglect of higher order terms in the spatial fluctuations needs to be consistent to those approximations applied in the derivation of the continuity, momentum and energy equations. Inserting a perturbation ansatz $\phi = \bar{\phi} + \phi'$, where $\bar{\phi}$ can be conveniently regarded as the time average, into Equations 13 and 14, and identifying the left hand side wave operator of the APE-4 system [20] with the unstable vorticity mode excluded, the perturbation equations in conservative non-dimensional form (in the following a special notation for non-dimensional quantities is omitted for clarity) read:

$$\begin{aligned} &\frac{\partial \epsilon \rho_s'}{\partial t} + \frac{\partial}{\partial x_k} \left(\bar{\rho} u_k' + \epsilon \bar{u}_k \rho_s' \right) - \frac{\epsilon}{\bar{c}^2} \left[2\epsilon\nu \frac{Ma_\infty}{DaRe_\infty} \bar{\rho} \bar{u}_i + 3 \frac{\epsilon^2 c_F}{\sqrt{Da}} |\mathbf{u}| \bar{\rho} \bar{u}_i \right] u_i' \\ &\qquad - \frac{|\bar{\mathbf{u}}|^2}{\bar{c}^2} \left[\epsilon\nu \frac{Ma_\infty}{DaRe_\infty} + \frac{\epsilon^2 c_F}{\sqrt{Da}} |\bar{\mathbf{u}}| \right] \rho_s' = \epsilon S_{\rho_s}, \end{aligned} \tag{15}$$

$$\frac{\partial u_i'}{\partial t} + \frac{\partial}{\partial x_k} \left(\bar{u}_k u_k' + \bar{c}^2 \frac{\rho_s'}{\bar{\rho}} \right) + \left[\epsilon\nu \frac{Ma_\infty}{DaRe_\infty} \delta_{ij} + \frac{\epsilon^2 c_F}{\sqrt{Da}} \left(\frac{\bar{u}_j \bar{u}_i}{|\mathbf{u}|} + |\mathbf{u}| \delta_{ij} \right) \right] u_j' = S_{u_i}, \tag{16}$$

where, for ease of notation, the angle brackets $\langle\ \rangle$ were omitted. Ma_∞ denotes the Mach number, $DaRe_\infty = Re_{d_p} \sqrt{Da}$ and c is the speed of sound. By the choice of variables the entropy mode is excluded as well. For the use in a conservative numerical scheme, the density fluctuation ρ_s' in an isentropic acoustic medium corresponding to the pressure fluctuations of the actual problem was introduced. According to the Euler assumption, namely vanishing viscous and thermal effects of the bulk fluid on wave propagation, all but the predominant Darcy and Forchheimer terms in the porous media are shifted to the right hand side source vector $(S_{\rho_s}, S_{\mathbf{u}})^T$, which includes moreover all higher order terms in the fluctuations. For aerodynamically induced noise, the source vector reduces

in good approximation to the Lamb vector. The additional acoustic attenuation from the interaction with the pore walls enters the modified APE-4 system through the Darcy terms, which scale by $\epsilon Ma_\infty / DaRe_\infty$ and the Forchheimer terms, which scale by $\epsilon c_F / \sqrt{Da}$. Note that in contrast to the flow quantities governed by the volume averaged Equations 6, 11 and 12, no apparent gradient terms acting solely at the interface appears at first sight, but as will be discussed in Chapter 2.3 the jumps in the acoustic quantities are encoded in the flux expressions. The system 15, 16 is solved by a high-order spectral element Discontinuous-Galerkin (DG) method [21].

The entire methodology is embedded in the in-house multiphysics solver ZFS, where in a directly coupled simulation both solvers run concurrently on a joint hierarchical Cartesian grid.

2.2.3. Model Analysis for Plane Waves

In the simplest case of a 1D wave propagation in the absence of mean flow, only the Darcy drag in Equation 16 is retained and the problem can be analyzed in frequency domain. Figure 2 shows several acoustical quantities, derived in the following. For a first sensitivity analysis the problem is considered in non-dimensionless form as a function of the least number of influence parameters, namely ϵ, Da and $Re_0 = Re_\infty / Ma_\infty$. Apart from the frequency the quantities depend either on $\epsilon / DaRe_0$ alone, or in case of the reflection coefficient R for instance also on ϵ. For reference realistic physical quantities for the problems presented in Chapter 3 are given alongside.
The parameter variation presented in Figure 2 can be taken from Table 1, where the permeability κ for fixed values of ϵ is exemplarily given. Complex quantities are displayed in terms of the amplitude and the phase. The analytical dispersion relation of the reduced system contains information regarding the complex, frequency dependent characteristic impedance:

$$Z(\omega) = \bar{\rho}\bar{c}\sqrt{1 - i\frac{\epsilon}{DaRe_0\omega}} \tag{17}$$

and the complex wave number (with the normalized characteristic impedance $\hat{Z}(\omega) = Z(\omega)/\bar{\rho}\bar{c}$):

$$k_p = \frac{\omega}{\bar{c}}\left\{\sqrt{\frac{1}{2}\left[|\hat{Z}(\omega)|^2 + 1\right]} - i\sqrt{\frac{1}{2}\left[|\hat{Z}(\omega)|^2 - 1\right]}\right\} \tag{18}$$

of plane wave solutions. In this limiting case of a mean flow at rest and remote from interfaces, the present model coincides with the model in [4], where the same expression for the complex wave number was obtained. According to Equation 17 acoustic waves in porous media exhibit a phase shift between pressure and particle velocity, already indicating that in case an acoustic wave hits the fluid-porous interface from the pure fluid, a reflected wave will be inevitably generated, to satisfy the impedance relation inside the porous media. For $\lim_{DaRe_0\omega\to\infty} Z(\omega) = Z_{fluid}$, i.e. large pore sizes or high frequencies, the behavior in pure fluid is restored. The real part of the complex wave number is illustrated in terms of the frequency dependent phase velocity $\omega/Re(k(\omega))$, normalized by the speed of sound in the pure saturating fluid c_f in Figure 2(c). Clearly, the speed of sound is lower than in the fluid and the acoustic wave propagation in the porous medium is dispersive. The acoustic attenuation is dictated by $\hat{p}(x)/\hat{p}(0) = \exp\{Im(k(\omega))x\}$ and shown in Figures 2(h) and 2(i) for two different $\epsilon/DaRe_0$-values.

To get the complex reflection and transmission coefficients for $\bar{\rho}, \bar{c} \in C^0(\partial\mathcal{B})$, the plane wave solutions in the pure fluid and pure porous regions are matched at the interface (compare Figure 2.3) via the relations:

$$u'_f = \epsilon_p u'_p \qquad \text{and} \qquad p'_f = p'_p \tag{19}$$

yielding:

$$R = \frac{\left(\frac{|\hat{Z}(\omega)|}{\epsilon_p}\right)^2 - 1 - i\frac{1}{\epsilon_p}\sqrt{2(|\hat{Z}(\omega)|^2 - 1)}}{\left(\frac{|\hat{Z}(\omega)|}{\epsilon_p}\right)^2 + 1 + \frac{1}{\epsilon_p}\sqrt{2(|\hat{Z}(\omega)|^2 + 1)}} \qquad \text{resp.} \qquad \lim_{DaRe_0\omega\to\infty} R = \frac{\frac{1}{\epsilon_p} - 1}{\frac{1}{\epsilon_p} + 1}. \tag{20}$$

Subscript $'f'$ indicates fluid quantities and $'p'$ the effective quantities in the porous media. The reflection is a function of the normalized impedance and the porosity ratio, as is the complex transmission coefficient $T = 1 + R$. This is illustrated in Figures 2(d) - 2(g) for $\epsilon = 1.0$ and $\epsilon = 0.8$ together with the limiting case, when $R(\epsilon_p, \omega)$ for $DaRe_0 \to 0$. Note, that $\lim_{f\to\infty} arg(R) = 0°$, $\forall\epsilon_p \in (0, 1)$, i.e. the phase shift is maximum for a certain frequency, which shifts to lower values for an increasing porous drag.

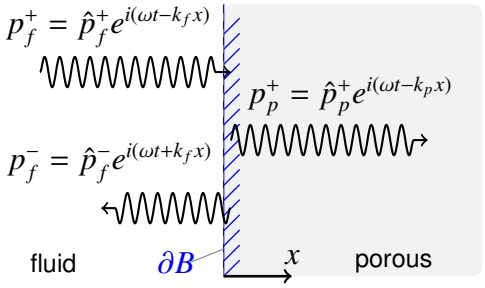

Figure 1: Incident, reflected and transmitted waves at the fluid-porous interface.

$\frac{\epsilon}{DaRe_0}$ \ ϵ	1.0	0.8	0.6	0.4
0.4 (——)	1.75	1.40	1.05	0.70
0.6 (– –)	1.17	0.93	0.70	0.47
0.8 (– · –)	0.88	0.70	0.53	0.35
1.0 (· · · ·)	0.70	0.56	0.42	0.28

Table 1: Permeability in 10^{-9} m^2 for different combinations of ϵ and Da for air with kinematic viscosity $\nu = 1.568 \cdot 10^{-5}$ m^2/s, speed of sound $c_f = 347$ m/s and characteristic length $L_{ref} = 15.5$ mm. The different linestyles refer to Figure 2.

3. EXPERIMENTAL CHARACTERIZATION OF MELAMINE FOAM

In the present section, the experimental setups considered for the analysis of melamine foam sound absorbing behavior and for the characterization of its properties are described. Moreover, the facility used to study anechoic transmission and reflection in a liner configuration is presented. The measurements have been conducted in collaboration with Centre de Transfert de Technologie du Mans (CTTM) and Laboratoire d'Acoustique de l'Université du Maine (LAUM).

3.3.1. Static air flow resistivity determination

For the determination of the static air flow resistivity, the measurement unit referred to the standard ISO 9053 has been exploited. σ is obtained by measuring the pressure gradient Δp on both sides of a sample through which a stabilized volume flow Q_v passes:

$$\sigma = \frac{\Delta p S}{Q_v l}, \tag{21}$$

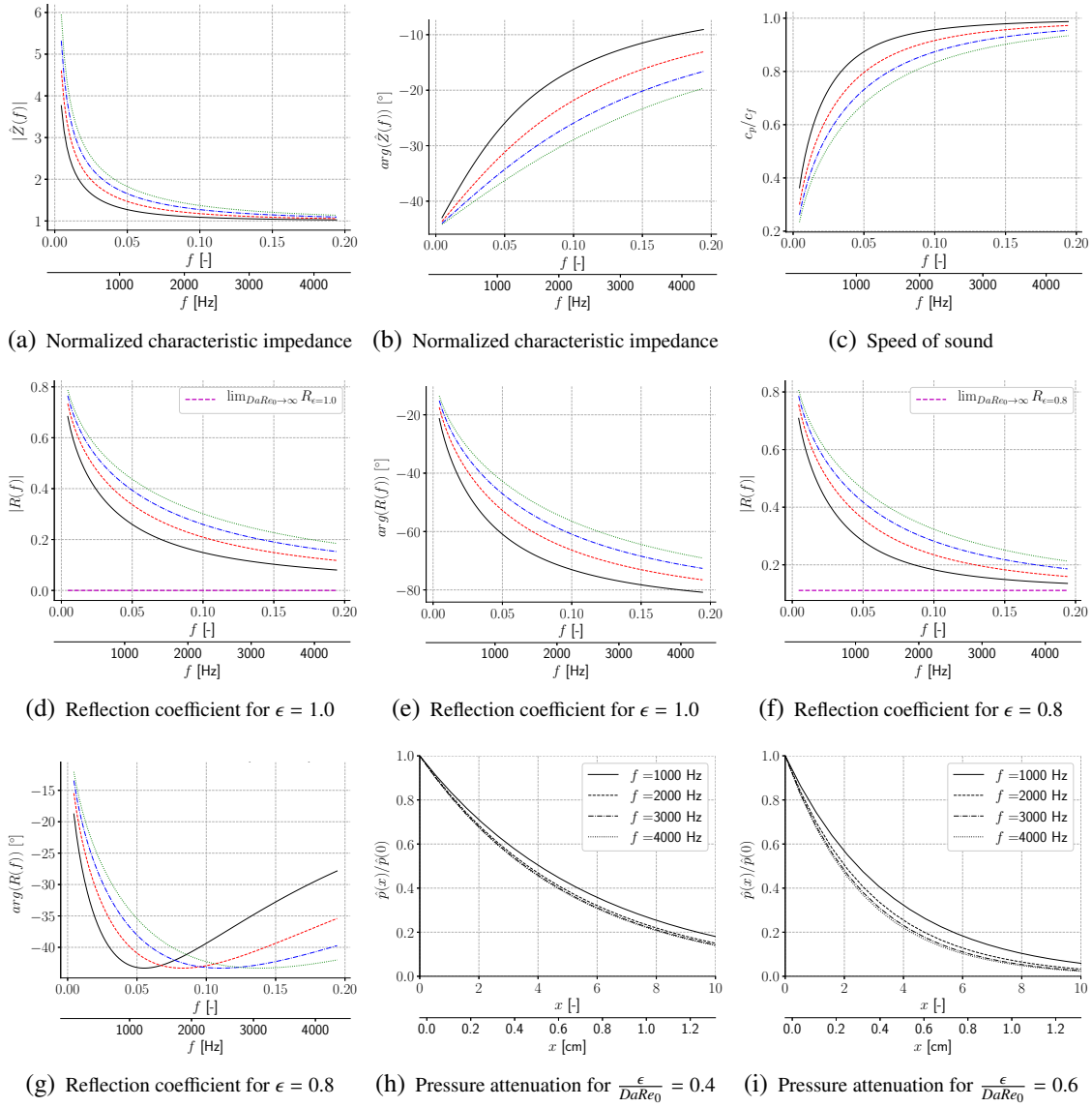

(a) Normalized characteristic impedance (b) Normalized characteristic impedance (c) Speed of sound

(d) Reflection coefficient for ϵ = 1.0 (e) Reflection coefficient for ϵ = 1.0 (f) Reflection coefficient for ϵ = 0.8

(g) Reflection coefficient for ϵ = 0.8 (h) Pressure attenuation for $\frac{\epsilon}{DaRe_0}$ = 0.4 (i) Pressure attenuation for $\frac{\epsilon}{DaRe_0}$ = 0.6

Figure 2: Acoustic quantities deduced from Equations 15 and 16 in case of plane waves. The non-dimensionalization and legend are given in Table 1.

where S is the cross section area of the sample and l is its length. Due to the anisotropic and inhomogeneous nature of melamine foam, three different cylindrical samples with a diameter of 44.5 mm and a thickness of 15.5 mm have been manufactured. The values of the static airflow resistivity for the different samples are 9215 Pa·s·m^{-2}, 8600 Pa·s·m^{-2} and 8233 Pa·s·m^{-2}, with an uncertainty of 700 Pa·s·m^{-2}. The retrieved parameters are in agreement with the typical range of values for the melamine foam (8000-12000 Pa·s·m^{-2}).

3.3.2. Sound absorption behavior analysis

In Figure 3 (configuration A) the setup for the determination of the sound absorbing behavior of the material by means of an impedance tube is depicted. A loudspeaker is placed at one side whereas the sample of the test material is at the opposite one. In the tube, a standing wave pattern is generated from a broadband stationary noise signal, being the result of a forward traveling sound wave and a backward (or reflected) sound wave. The frequency of the sound signal is kept lower than the cut-off frequency of the

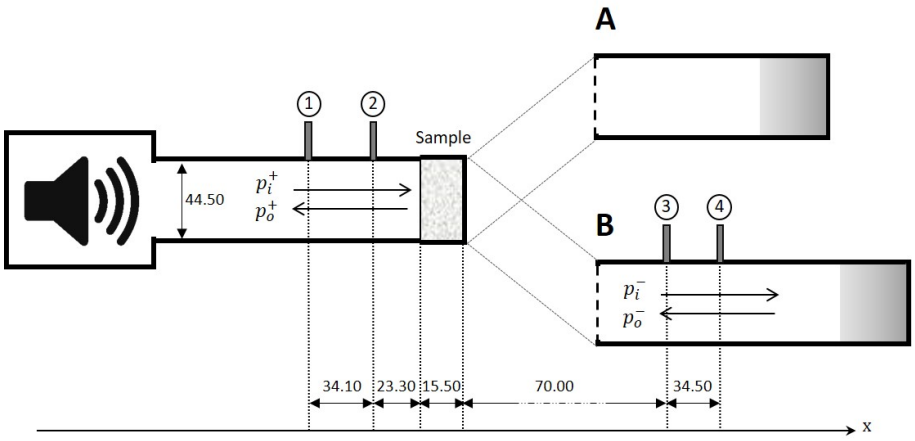

Figure 3: Configurations of the impedance tube for the determination of the sound absorbing behavior (A) and the characterization of the pore parameters (B) of melamine foam. The distances are expressed in mm.

tube to assure the generation of plane propagating waves. Two fixed microphones are located at two different positions in the tube wall. The method, labeled as *2p method* [22,23], is based on the estimation of the transfer function between the microphones. The measurement of the transfer function allows the mathematical separation of incident and reflected waves, leading to the anechoic reflection coefficient R of the sample for the same frequency band of the broadband signal. The normalized characteristic impedance Z and absorption coefficient α can be derived by:

$$\hat{Z} = \frac{1+R}{1-R}; \qquad \alpha = 1 - R^2. \tag{22}$$

For the measurement, a white noise signal is emitted by the loudspeaker with a frequency range of 50-5000 Hz, whereas the range considered for the acquisition is 80-4300 Hz. The sampling frequency is set to 51200 Hz.

3.3.3. Characterization of melamine foam parameters

The impedance tube in Figure 3 has been set up for a second measurement with four microphones (configuration B) with the aim of determining the porous model parameters through the inverse characterization method developed by Niskanen et al. [24]. The technique consists of fitting the JCAL model describing the porous medium to the measurement of the scattering matrix, which contains the anechoic reflection, R, and the anechoic transmission, $T' = Te^{ikL}$, of the material, L being the thickness of the considered sample. The inversion is performed in the Bayesian framework. T' and R can be expressed by:

$$T' = \frac{p_o^- p_i^+ - p_o^+ p_i^-}{(p_i^+)^2 - (p_i^-)^2}; \qquad R = \frac{p_o^+ p_i^+ - p_o^- p_i^-}{(p_i^+)^2 - (p_i^-)^2}. \tag{23}$$

The considered excitation signal is a logarithmic swept sine, over the frequency range of 100–4300 Hz, in order not to overcome the cut-off frequency of the tube ($\sim$ 5 kHz). The microphones have been first calibrated and phase matched with each other to enhance the accuracy of the results. The pore parameters obtained for the samples for the frequency range of 800-5500 Hz are listed in Table 2 and have been also used as inputs for the JCAL

model in order to compare the experimental absorption coefficient with the analytical predictions.

Table 2: JCAL model parameters characterizing the melamine foam

ϵ [-]	α_∞ [-]	Λ [m]	Λ' [m]	κ_0 [m^2]	κ_0'[m^2]
0.986	1.02	$1.344 \cdot 10^{-4}$	$1.942 \cdot 10^{-4}$	$1.410 \cdot 10^{-9}$	$2.382 \cdot 10^{-9}$

3.3.4. Liner configuration

A scheme of the setup prepared for studying the effects of the flow on the transmission and the reflection of the sound waves in the porous media is shown in Figure 4. The melamine foam sample has been cut in the form of a 200 mm x 100 mm rectangular plate with a thickness of 15.5 mm and flush mounted in a metallic box, forming a liner configuration that is placed in a wind tunnel and that is held in position by a series of metallic bars having the same thickness of the plate.

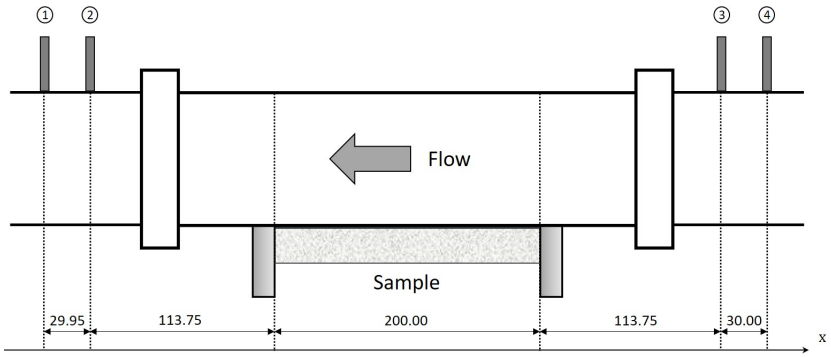

Figure 4: Scheme of the melamine foam sample flush-mounted on the wind tunnel wall. The distances are expressed in mm.

The box containing the samples is placed in the central part of the wind tunnel. In order to avoid acoustic reflection, the tunnel is equipped with anechoic terminations. Two B&K microphones are placed at each side of the liner. A loudspeaker is located upstream of the sample and emits a logarithmic swept sine over the frequency range of 100–4300 Hz. Its position can be modified in order to invert the direction of the sound propagation in relationship to the position of the sample. The flow goes from the right to the left of the tunnel. The comparison between the signal recorded by the upstream microphones and the ones downstream of the sample leads to the estimation of anechoic transmission and reflection. A possible way to measure the matrices has been reviewed by Åbom [25]. The test has been conducted in absence of flow and with a flow velocity of about 30.5 m/s.

4. MODEL EVALUATION

Hereinafter, the low velocity limit, where inertia effects expressed by the Forchheimer term are negligible, i.e. the low permeability Reynolds number Re_d limit, will be considered. The data from the experiments will be used to evaluate the predictive behavior of the porous model from Chapter 2.

4.4.1. Flow resistivity test

For the reduced model, the experimental data can be used to make a priori estimation of the permeability or the Darcy number, respectively, from the (static) flow resistivity σ with the simplifying assumption of a top-hat velocity profil. With view on Equation 9 the linear Darcy drag scales by the local flow velocity inside the porous layer. Assuming a constant pressure drop and an isothermal flow an appropriate mean velocity can be derived to be $\bar{u} \approx \frac{\rho u}{\Delta \rho} \ln(u_{lp}/u_{rp})$, where u_{lp} and u_{rp} denote the velocities at the left and right edges of the porous sample and from that the permeability (Da) has been estimated to be $\kappa = 2.12 \cdot 10^{-9}$ m^2 ($Da = 8.82 \cdot 10^{-6}$) for a mean $\bar{\sigma} = 8683$ Pa·s· m^{-2}. This has been confirmed by a simple laminar channel simulation and used to validate the implementation.

4.4.2. Impedance tube

In the numerical simulations, for the purpose of efficiency, the loudspeaker was modeled by a superposition of multiple harmonics, and weakly enforced at the inlet boundary, which for plane waves is non-reflecting for outgoing waves. The number of harmonics are chosen to avoid an interference among adjacent frequency components, due to the finite resolution of the frequency content, following the total acquisition interval. The data acquisition for the DFT includes a time span of an integral multiple of the lowest frequency component, to avoid windowing and thus a blurring of the spectrum due to spectral leakage. The time domain signals are post processed via a FFT, to get the acoustic responses in frequency domain. The porous sample was resolved by 51 elements and a fourth-order discretization was used.
Since the mathematical problem of a sound wave propagating in a duct can be considered one-dimensional for frequencies up to the cut-off frequency, the total sound pressure at any point in the tube can be expressed by:

$$P(x) = Ae^{-ikx} + Be^{ikx}. \tag{24}$$

The transfer function between the two microphones, indicated by the subscripts 1 and 2, is:

$$H_{12} = \frac{P(x_2)}{P(x_1)} = \frac{Ae^{-ikx_2} + Be^{ikx_2}}{Ae^{-ikx_1} + Be^{ikx_1}} = \frac{e^{-ikx_2} + Re^{ikx_2}}{e^{-ikx_1} + Re^{ikx_1}}, \tag{25}$$

where $R = {}^{B}/_{A}$ is the pressure reflection coefficient, which follows from:

$$R = \frac{e^{-ikx_2} - H_{12}e^{-ikx_1}}{H_{12}e^{ikx_1} - e^{ikx_2}}. \tag{26}$$

The results for the sound absorption coefficient Equation 22 are shown in Figure 5(a) for the three samples from the experiments and the numerical simulations, performed for three different permeabilities. $\kappa = 2.12 \cdot 10^{-9}$ m^2 belongs to the value as retrieved from the flow resistivity test and obviously underpredicts the acoustic absorption. This is however in accordance to the deviating values of σ as deduced from the static pressure drop measurements and the JCAL model parameters as retrieved by inverting acoustic measurement data, where the viscous permeability κ_0 is related to the flow resistivity σ by $\kappa_0 = {}^{\eta}/_{\sigma}$ and yields a static air flow resistivity of $\approx$ 13000 Pa·s·m^{-2} (compare Table 2). The molecules in a longitudinal acoustic wave carry out a dynamic forth and back movement, as opposed to the in average steady directional movement of the molecules in a steady laminar flow, such that it assumed that at the pore-scales, the interaction between

the fluid and the rigid frame might obey different mechanisms (see also [5]). This justifies a separate calibration of the Darcy model by means of the acoustic measurements for the wave propagation simulation rather than adapting κ from the static flow measurement. In this way, a third curve for $\kappa = 0.84 \cdot 10^{-9}$ m^2 was obtained. Especially, at lower frequencies the Darcy model still deviates from the experiments, which is currently investigated.

Note, that the absorption is a consequence of the acoustic attenuation by the porous layer, the reflection and transmission at the first fluid-porous layer and the interaction with the solid back plate. Therefore, further simulations for slightly varying sample thicknesses (+3% and +6%) and air gaps of the cavity between the sample and the back plate are shown in Figures 5(b) and 5(c) for $\kappa = 0.84 \cdot 10^{-9}$ m^2, to predict the sensitivity. Increasing the sample thickness enhances the absorption, similar to an increase in gap size, which can be attributed to the Helmholtz resonance effect [26].

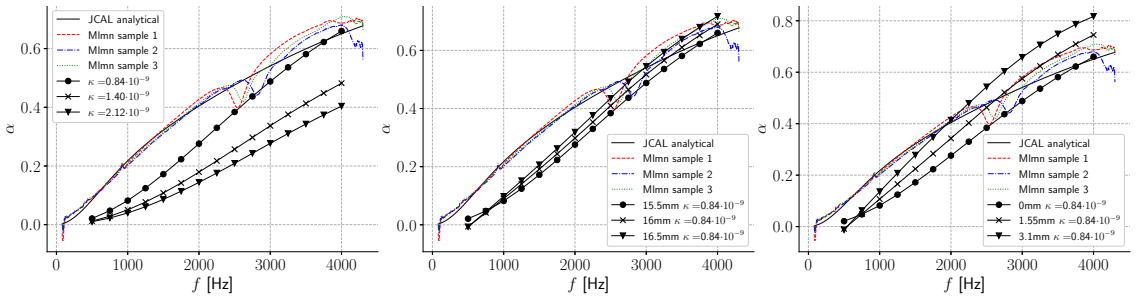

(a) Different permeabilities of the model (b) Different sample thicknesses (c) Different gap sizes

Figure 5: Sound absorption coefficient for the three samples of the experiment, for different configurations in the simulations, indicated by markers, and the JCAL model fitted to experimental data.

4.4.3. Acoustic liner configuration

In this setup the incoming plane acoustic waves get diffracted at the edge and can penetrate the porous medium, where they get attenuated. Additionally, waves are reflected at both ends of the box, containing the porous sample, where a standing wave can form. In the numerical simulations the excitation was implemented similarly to the impedance tube, but this time both ends were equipped with non-reflecting boundary conditions. Here, the porous layer was discretized by 41 elements. The acoustic quantities have been observed to be unaffected by a further mesh refinement. For all subsequent simulations the optimal value of $\kappa = 0.84 \cdot 10^{-9}$ m^2 was used. In the first of the three configurations considered, without mean flow (i.e. $\bar{u} = 0$ m/s), only one layer of melamine foam was placed. In the following the results are juxtaposed in terms of the anechoic transmission coefficient, as introduced in Chapter 3.3, in Figure 6. $()^+$ and $()^-$ refer in the experiments to the upstream and downstream positions of the loudspeaker, respectively, which should coincide for $\bar{u} = 0$ m/s because of the symmetry of the setup. The numerical model predicts the same trend, but with an offset to a larger transmission of the incoming waves, suggesting the acoustic liner to be less effective.
In the second configuration with mean flow ($\bar{u} = 30$ m/s), the convection effect was considered. For this case the mean flow field was computed by means of Equations 6, 11 and 12 beforehand. The instantaneous vorticity field and the velocity profils at two locations over the height of the channel are shown in Figure 7. The mounted sample in liner configuration abruptly expands the cross-sectional area and the hard solid

termination for the flow by the the no-slip boundary is replaced by a permeable layer, which allows the partial intrusion of the fluid. It enables the formation of vorticities at the fluid-porous shear layer. This is illustrated by the left velocity profile in Figure 7(b), where a vortex is passing by. The mean flow field was used to predict the wave propagation in the second CAA step. No other acoustic sources other than the loudspeaker have been considered. Again an offset is observed between measurements and the simulation. In both cases, the transmission is enhanced by the flow when it goes in the same direction of the sound wave propagation of the signal emitted by the loudspeaker. Only for very high frequencies the behavior is shifted, which is more pronounced in the simulations.

The maximum attenuation occurs at high frequencies and is also related to the thickness of the porous media. For this reason, the minimum of the curve can be moved by acting on the samples. A second layer of melamine foam with a thickness of 15.5 mm and $\bar{u} = 0$ m/s was considered in the third test case, to further evaluate the predictive behavior of the simulations. In this case the maximum attenuation occurs at about 2750 Hz in both, the experiments and the simulations, but for even higher frequencies the model underestimates the transmission.

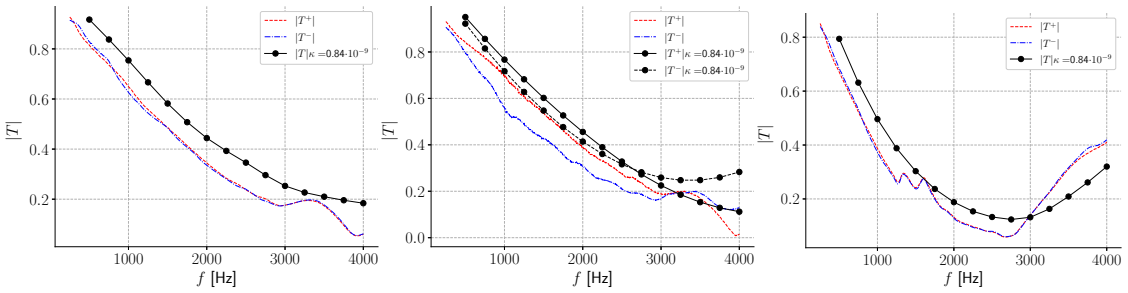

(a) $\bar{u}$ = 0m/s (b) $\bar{u}$ = 30m/s (Ma_∞ = 0.09) (c) Double smaple

Figure 6: Transmission coefficients for the acoustic liner configuration of the experimental measurements, the fitted JCAL model and for different configurations of the simulations. $()^+$ *and* $()^-$ *indicate the two loudspeaker positions, upstream and downstream of the tube.*

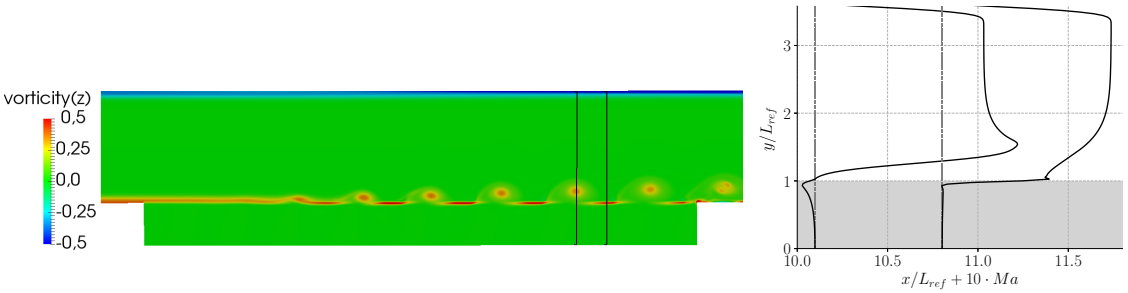

(a) Vorticity field (b) Double sample

Figure 7: 7(a) shows the instantaneous vorticity, where the porous section extends from $x/L_{ref} = 0$ *to* $x/L_{ref} = 12.9$*. In 7(b) the velocity profiles at two locations indicated in 7(a) by solid lines are given. The shaded area corresponds to the porous layer.*

5. CONCLUSIONS

In the present work, a numerical model for the simulation of porous media was presented, both to predict the flow field and acoustic wave propagation via the extended APE system. The focus was on the later and the modifications due to the Darcy drag term in the limit of low permeability Reynolds numbers. A theoretical analysis for the plane wave case completed the derivation. The comparison of the model to experiments and the JCAL model, which has been fitted to the experimental data, had been exemplarily shown by means of the absorption coefficient in an impedance tube and the transmission of acoustic waves inside an acoustic liner configuration. Both experiments and simulations, suggest a separate calibration of the model for the use in a CFD simulation and in a CAA simulation. In general, the tendencies are qualitatively well captured, but with an offset indicating the numerical model to be less sound absorbing. The challenges arise from acoustic quantities most suitably described in frequency-domain, but the need for an equivalent acoustic response in models of time-marching schemes. This makes it harder to match the experiments over a large frequency range.

ACKNOWLEDGEMENTS

This project has received funding from the European Union's Horizon 2020 research and innovation programme under the Marie Skłodowska-Curie grant agreement No. 722401 and is part of the IMAGE project (Innovative Methodologies and technologies for reducing Aircraft noise Generation and Emission), which is a EU-China collaborative project, funded, for EU partners, by the European Community in the H2020 programme under Contract No. 688971-IMAGE and, for Chinese participants, by the MIIT of China. The authors also gratefully acknowledge the Gauss Centre for Supercomputing e.V. (www.gauss-centre.eu) for funding this project by providing computing time on the GCS Supercomputer HAZEL HEN at Höchstleistungsrechenzentrum Stuttgart (www.hlrs.de).

REFERENCES

[1] WP Breugem, BJ Boersma, and RE Uittenbogaard. The influence of wall permeability on turbulent channel flow. *Journal of Fluid Mechanics*, 562:35–72, 2006.

[2] Seong Ryong Koh, Beckett Zhou, Matthias Meinke, Nicolas Gauger, and Wolfgang Schröder. Numerical analysis of the impact of variable porosity on trailing-edge noise. *Computers & Fluids*, 167:66–81, 2018.

[3] Beckett Y Zhou, Seong Ryong Koh, Nicolas R Gauger, Matthias Meinke, and Wolfgang Schöder. A discrete adjoint framework for trailing-edge noise minimization via porous material. *Computers & Fluids*, 172:97–108, 2018.

[4] Benjamin W Fassmann, Christof Rautmann, Roland Ewert, and Jan Delfs. Prediction of porous trailing edge noise reduction via acoustic perturbation equations and volume averaging. In *21st AIAA/CEAS Aeroacoustics Conference*, page 2525, 2015.

[5] Kirill V Horoshenkov. A review of acoustical methods for porous material characterisation. *Int. J. Acoust. Vib*, 22(1):92–103, 2017.

[6] David Linton Johnson, Joel Koplik, and Roger Dashen. Theory of dynamic permeability and tortuosity in fluid-saturated porous media. *Journal of Fluid Mechanics*, 176:379–402, March 1987.

[7] Donald A Drew. Mathematical modeling of two-phase flow. *Annual review of fluid mechanics*, 15(1):261–291, 1983.

[8] Stephen Whitaker. Theory and applications of transport in porous media: The method of volume averaging. *The Netherlands: Kluwer Academic Publishers*, 1999.

[9] WP Breugem and BJ Boersma. Direct numerical simulations of turbulent flow over a permeable wall using a direct and a continuum approach. *Physics of fluids*, 17(2):025103, 2005.

[10] J Alberto Ochoa-Tapia and Stephen Whitaker. Momentum transfer at the boundary between a porous medium and a homogeneous fluid—i. theoretical development. *International Journal of Heat and Mass Transfer*, 38(14):2635–2646, 1995.

[11] Wilhelmus Paulus Breugem. The influence of wall permeability on laminar and turbulent flows: Theory and simulations. 2005.

[12] Stephen Whitaker. Flow in porous media i: A theoretical derivation of darcy's law. *Transport in porous media*, 1(1):3–25, 1986.

[13] Stephen Whitaker. The forchheimer equation: a theoretical development. *Transport in Porous media*, 25(1):27–61, 1996.

[14] Daniel Hartmann, Matthias Meinke, and Wolfgang Schröder. An adaptive multilevel multigrid formulation for cartesian hierarchical grid methods. *Computers & Fluids*, 37(9):1103–1125, 2008.

[15] Daniel Hartmann, Matthias Meinke, and Wolfgang Schröder. A strictly conservative cartesian cut-cell method for compressible viscous flows on adaptive grids. *Computer Methods in Applied Mechanics and Engineering*, 200(9-12):1038–1052, 2011.

[16] Lennart Schneiders, Daniel Hartmann, Matthias Meinke, and Wolfgang Schröder. An accurate moving boundary formulation in cut-cell methods. *Journal of Computational Physics*, 235:786–809, 2013.

[17] Michael Moessner and Rolf Radespiel. Numerical simulations of turbulent flow over porous media. In *21st AIAA Computational Fluid Dynamics Conference*, page 2963, 2013.

[18] Michael Mößner and Rolf Radespiel. Modelling of turbulent flow over porous media using a volume averaging approach and a reynolds stress model. *Computers & Fluids*, 108:25–42, 2015.

[19] Sutharsan Satcunanathan, Matthias Meinke, and Schröder Wolfgang. Prediction of noise mitigation by porous media based on a hybrid cfd/caa method. In *25th AIAA/CEAS Aeroacoustics Conference*, accepted, 2019.

[20] Roland Ewert and Wolfgang Schröder. Acoustic perturbation equations based on flow decomposition via source filtering. *Journal of Computational Physics*, 188(2):365–398, 2003.

[21] Michael Schlottke-Lakemper, Hans Yu, Sven Berger, Matthias Meinke, and Wolfgang Schröder. A fully coupled hybrid computational aeroacoustics method on hierarchical cartesian meshes. *Computers & Fluids*, 144:137–153, 2017.

[22] J. Y. Chung and D. A. Blaser. Transfer function method of measuring in-duct acoustic properties. i. theory. *The Journal of the Acoustical Society of America*, 68(3):907–913, September 1980.

[23] J. Y. Chung and D. A. Blaser. Transfer function method of measuring in-duct acoustic properties. ii. experiment. *The Journal of the Acoustical Society of America*, 68(3):914–921, September 1980.

[24] M. Niskanen, J.-P. Groby, A. Duclos, O. Dazel, J. C. Le Roux, N. Poulain, T. Huttunen, and T. Lähivaara. Deterministic and statistical characterization of rigid frame porous materials from impedance tube measurements. *The Journal of the Acoustical Society of America*, 142(4):2407–2418, October 2017.

[25] Mats Åbom. Measurement of the scattering-matrix of acoustical two-ports. *Mechanical Systems and Signal Processing*, 5(2):89–104, March 1991.

[26] Michael Peter Norton and Denis G Karczub. *Fundamentals of noise and vibration analysis for engineers*. Cambridge university press, 2003.